

A New Global Ionospheric Electron Density Model Based on Grid Modeling Method

Huijun Le¹, Tingwei Han², Libo Liu³, Yiding Chen¹, and Hui Zhang¹

¹Institute of Geology and Geophysics, Chinese Academy of Sciences

²institute of Geology and Geophysics, CAS

³Key Laboratory of Earth and Planetary Physics, Institute of Geology and Geophysics, Chinese Academy of Sciences

November 24, 2022

Abstract

Based on nearly 4.6 million radio occultation ionospheric profile data from COSMIC satellites in 2006-2020, a global three-dimensional ionospheric electron density model was constructed by a new concept. The global 3D ionosphere structure was divided into total 338,661 grids with longitude intervals of 10 degrees, latitude intervals of 2 degrees, and height intervals of 5 km. Each individual grid model is first constructed, and then all grid models are combined to form a global ionospheric model. Each grid model has 21 coefficient for modeling solar activity, geomagnetic activity, local time, and season variation. This method makes full use of all ionospheric electron density data without any spatial smoothing, and can effectively model the fine ionospheric spatial structure like longitudinal wavenumber-4 structure in low latitudes. The model also takes into account the influence of both solar and geomagnetic activities on the ionosphere. It can give the climatological variation of ionospheric electron density with geomagnetic activity. In addition, by combined with the International Reference Ionospheric electron density results of E layer below 140km, the problem of three-peak error of occultation data below peak height of F2 layer in middle and low latitude region is effectively solved, and accurate low-altitude profile data can be obtained. Compared with other data sources such as ZH01 and ROCSAT-1, the simulation ability of the model in fine spatial structure is verified.

Hosted file

essoar.10509845.1.docx available at <https://authorea.com/users/541486/articles/603266-a-new-global-ionospheric-electron-density-model-based-on-grid-modeling-method>

1 **A New Global Ionospheric Electron Density Model Based on Grid**

2 **Modeling Method**

3 **Huijun Le^{1,2,3,5}, Tingwei Han^{1,2,5}, Libo Liu^{1,2,3,5}, Yiding Chen^{1,2,4,5}, Hui Zhang^{1,2,3,5}**

4 ¹ Key Laboratory of Earth and Planetary Physics, Institute of Geology and
5 Geophysics, Chinese Academy of Sciences, Beijing, 100029, China

6 ² Institutions of Earth Science, Chinese Academy of Sciences

7 ³ Mohe National Geophysical Observatory, Institute of Geology and Geophysics,
8 Chinese Academy of Sciences, Beijing, 100029, China

9 ⁴ Beijing National Observatory of Space Environment, Institute of Geology and
10 Geophysics, Chinese Academy of Sciences, Beijing, 100029, China

11 ⁵ College of Earth and Planetary Sciences, University of the Chinese Academy of
12 Sciences, Beijing 100049, China

13 Corresponding author: Huijun Le (lehj@mail.iggcas.ac.cn)

14
15
16 **Key Points:**

- 17 • A new global ionosphere empirical modeling method is proposed.
- 18 • Global modeling is decomposed into three-dimensional grid-point independent
19 modeling
- 20 • The new model can effectively preserve the regional differences of ionosphere

21

22 **Abstract:**

23 Based on nearly 4.6 million radio occultation ionospheric profile data from COSMIC
24 satellites in 2006-2020, a global three-dimensional ionospheric electron density model
25 was constructed by a new concept. The global 3D ionosphere structure was divided
26 into total 338,661 grids with longitude intervals of 10 degrees, latitude intervals of 2
27 degrees, and height intervals of 5 km. Each individual grid model is first constructed,
28 and then all grid models are combined to form a global ionospheric model. Each grid
29 model has 21 coefficient for modeling solar activity, geomagnetic activity, local time,
30 and season variation. This method makes full use of all ionospheric electron density
31 data without any spatial smoothing, and can effectively model the fine ionospheric
32 spatial structure like longitudinal wavenumber-4 structure in low latitudes. The model
33 also takes into account the influence of both solar and geomagnetic activities on the
34 ionosphere. It can give the climatological variation of ionospheric electron density
35 with geomagnetic activity. In addition, by combined with the International Reference
36 Ionospheric electron density results of E layer below 140km, the problem of
37 three-peak error of occultation data below peak height of F2 layer in middle and low
38 latitude region is effectively solved, and accurate low-altitude profile data can be
39 obtained. Compared with other data sources such as ZH01 and ROCSAT-1, the
40 simulation ability of the model in fine spatial structure is verified.

41 **1. Introduction**

42 The Earth's ionosphere is full of charged particles, which can reflect and modify
43 radio waves used for radio communication, navigation, and operation of the satellite
44 navigation systems like GPS, GLONASS, BEIDOU, and GALILEO. The ionosphere
45 is also the most closely region related to human activities in space. Many of our
46 Earth-orbiting satellites hang out there, including the International Space Station
47 and China Space Station. these satellites add spacecrafts can also be affected by the
48 various changes in the ionosphere, including sudden swells of charged particles that
49 increase drag on satellites and shorten their orbital lifetimes. Therefore, there is a
50 growing demand for understanding and forecasting the ionosphere. The ionosphere is
51 affected by solar radiation, solar wind, geomagnetic storms, as well as the energy
52 propagating upward from lower atmosphere. The ability to model and eventually
53 anticipate the solar cycle, annual, semi-annual and seasonal variations as well as
54 irregularities in ionosphere is of great use for both ionospheric research and space
55 weather applications. A variety of ground-based and space-based detection devices
56 have been developed internationally, and many local and global ionospheric empirical
57 models have been constructed based on these observations (e.g. Gowtam et al., 2019;
58 Hoque and Jakowski, 2011; Li et al., 2021; Kutiev et al., 2009; Le et al., 2017;
59 Themens et al., 2017).

60 Since the 1990s, GPS has been gradually applied to ionospheric
61 observations. The time delay and phase shift obtained by the dual-frequency receiver
62 can obtain a high accuracy of the total ionospheric electron content. With the increase
63 of ground-based GPS receivers, these rich ionospheric observations have greatly
64 improved our understanding and knowledge of the ionosphere. Many ionospheric
65 empirical models are also constructed based on these GPS/TEC data. The GPS/TEC
66 method also has some limitations. On the one hand, it can only get the total integrated
67 electron content without the electron density height profile information. On the other
68 hand, due to the limitations of topography, the receiver can only be placed on land, so
69 a large number of data over the ocean are missing. The application of radio
70 occultation technology in atmospheric and ionospheric detection can effectively

71 remedy the above two deficiencies. On the one hand, the information of ionospheric
72 electron density height profile can be obtained by occultation method, although there
73 are some errors in low altitude. On the other hand, occultation observations are not
74 affected by topography and has good global coverage.

75 According to the characteristics of ionospheric observation data, there are many
76 methods to construct regional or global empirical model of ionospheric electron
77 density, including spherical harmonic function method, empirical orthogonal function,
78 custom fitting function, etc. All of these methods perform a degree of fitting and
79 smoothing of the observed data and may therefore lose some local features. If the
80 globe is evenly divided into sufficiently fine grids, and there is enough data in each
81 grid to create a separate model for each grid, then the grid models can be aggregated
82 to form a global ionospheric model. This is a new concept of ionospheric empirical
83 modeling. This new grid modeling method can make full use of all observation
84 information and avoid using the same function to fit all latitude and longitude data.
85 That is, this method can effectively preserve the regional differences of ionosphere. If
86 we have enough data in global range, we can use this method to construct a high
87 accuracy model. We name this method as Grid Modelling.

88 The Constellation Observing System for Meteorology, Ionosphere, and Climate
89 (COSMIC) is a constellation of six small satellites that study Earth's atmosphere and
90 ionosphere. These satellites were launched in 2006 and then continue operate until now.
91 The electron density profiles derived from the occultation observations have reached
92 more than 4.6 million. These data are enough for us to carry out Grid Modeling.

93 **2. Data Source**

94 The COSMIC occultation data were used in this ionospheric empirical modeling
95 work. The electron density height profiles can be calculated by Radio Occultation
96 method. The COSMIC electron density data cover long time of more than one solar
97 cycle from 2006 to 2019. The electron density height profiles of total 4.6 million were
98 used in the modeling work. For each ionospheric electron density height profile,
99 electron density at various heights from 140 km to 700 km with 5 km interval were
100 interpolated. Thus the ionosphere is binned into 113 heights. At each fixed height,

101 there are about 4.6 million electron density data. Then we can get about 520 million
102 data points. These data have good coverage in longitude, latitude, local time, season,
103 solar activity, geomagnetic activity and so on. Figure 1 shows the distribution of the
104 COSMIC electron density data in these respects.

105 Solar radiation flux at 10.7cm band was used to characterize solar activity. F107
106 is a daily solar activity index used as an input parameter in many ionospheric
107 empirical and theoretical models (e.g., Hedin et al., 1996; Picone et al., 2002;
108 Titheridge, 1997; Yue et al., 2008) to represent changes in solar activity. F107A is the
109 81-day moving average value of daily F107 index. F107P is the mean value of daily
110 F107 and its 81-day moving average F107A. The F107P index has been verified to be
111 a better solar EUV proxy for ionosphere modeling and ionospheric investigations (e.g.
112 Liu et al., 2006, 2009; Ma et al., 2009; Ikubanni and Adeniyi, 2017). Thus, the F107P
113 index is used here to model solar activity variation of ionospheric electron density. In
114 addition, the Kp index is used here to model geomagnetic activity variations of
115 ionospheric electron density.

116 To verify the model results, we also selected the radio occultation data of China
117 Seismo-Electromagnetic Satellite/ZhangHeng-01 (CSES / ZH01) with a similar orbit
118 height to COSMIC. The orbit locates at an altitude of about 507 km. The CSES
119 satellite was launched on Feb 2, 2018. It has a Sun-synchronous orbit. Its
120 descending/ascending node is at 1400 LT/0200 LT. The CSES radio occultation data
121 only cover the low solar activity period of 2018-2020. We also selected the total ion
122 density data of ROCSAT-1 satellite to check the IGGM model results with non radio
123 occultation data. ROCSAT-1 was launched on January 27, 1999. Its orbit height was
124 600 km and its orbit inclination was 35°. Thus it can only cover the low latitudes
125 within $\pm 35^\circ$. The ionospheric plasma and electrodynamics instrument (IPEI) onboard
126 the satellite consists of four sensors to measure the ion concentration, the ion
127 temperature, and the ion drift velocity vector. Here we used the data of total positive
128 ion density which is basically equal to electron density according to the principle of
129 electric neutrality of ionosphere charged particles.

130 **3. Model Construction**

131 The model constructed in this paper is based on the Grid Modeling approach, so
 132 the model is named Ionosphere Global Grid Model (IGGM). To simulate the global
 133 ionospheric electron density variation, we divide the globe into many grids according
 134 to longitude, latitude and height, and model each grid point separately. The global
 135 ionosphere is divided into 37 longitude planes (from -180 degrees to 180 degrees with
 136 10 degrees interval), 81 latitude zones (from -80 degrees to 80 degrees with 2 degrees
 137 interval) and 113 heights in altitude (from 140 km to 700 km with 5 km
 138 interval). There are total of 338,661 grid points in the global ionosphere model. Figure
 139 2 illustrates the grid distribution of the model.

140 The ionospheric electron density was modeled for each grid point. First of all, all
 141 electron density data near the grid point (The longitudinal range is ± 7.5 degrees and
 142 latitudinal range is ± 2 degrees) are selected as the observation data of the grid point.
 143 There are 4.6 million observations worldwide, with approximately 4,800 observations
 144 at each grid point. The model of each grid point can then be constructed based on the
 145 fitting method. Because we have decomposed global ionospheric modeling into
 146 sufficiently fine grid modeling, the modeling for each grid mainly simulates solar
 147 activity, geomagnetic activity, seasonal and local time variations. The model equation
 148 is as follows:

$$149 \quad \begin{cases} Ne_{global} = \cup Ne_{ijk}, & Ne_{ijk} = A_{n1} \cdot A_{n2} \cdot A_{n3} \\ A_{n1} = c_{n11} + c_{n12} \cdot F107P + c_{n13} \cdot F107P^2 + c_{n14} \cdot Kp + c_{n15} \cdot Kp^2 \\ A_{n2} = 1 + \sum_{m=1}^4 c_{n21m} \cdot \cos\left(\frac{2\pi \cdot m \cdot DOY}{365}\right) + c_{n22m} \cdot \sin\left(\frac{2\pi \cdot m \cdot DOY}{365}\right) \\ A_{n3} = 1 + \sum_{m=1}^4 c_{n31m} \cdot \cos\left(\frac{2\pi \cdot m \cdot LT}{24}\right) + c_{n32m} \cdot \sin\left(\frac{2\pi \cdot m \cdot LT}{24}\right) \end{cases} \quad (1)$$

150 The Ne_{ijk} is the electron density model at a fixed grid of longitude i , latitude j and
 151 altitude k ($i=1, \dots, 37$; $j=1, \dots, 81$; $k=1, \dots, 113$). The A_{n1} , A_{n2} and A_{n3} represent
 152 the solar cycle & geomagnetic variation, seasonal variation and local time variation,
 153 respectively (e.g., Xu and Kamide, 2004; Ercha et al., 2012; Le et al., 2017). For each
 154 grid model, we calculated values of the 21 coefficients in the formula above through
 155 solving nonlinear curve-fitting problems in least-squares sense. The global model

156 IGGM have total of 7,111,881 coefficients. Based on these coefficients, we can
157 calculate the three-dimensional distribution of global ionospheric electron density for
158 a given solar activity, geomagnetic activity, season, local time/universal time.
159 Meanwhile, peak density NmF2, peak height hmF2 and total electron content (from
160 140 km to 700km) can also be calculated.

161 Abel Inversion of ionospheric electron density height profile by radio occultation
162 requires some assumption (Schreiner et al., 1999; Let al., 2007; Straus, 2007; Yue et
163 al., 2010), including spherical symmetric distribution of electron density, straight line
164 signal propagation, and first order estimate of the electron density at the top.
165 Spherical symmetry assumption is thought to be the major error source (Straus et al.,
166 2007). In fact, ionospheric electron density is not symmetrically distributed, and the
167 asymmetry is more pronounced at lower latitudes (et al. Straus, 2007; Yue et al.,
168 2010). Therefore, the COSMIC electron density data has a large error below the peak
169 height at low latitudes (e.g. Yue et al., 2011). It is well known that ionosphere electron
170 density has a significant two-peak EIA structure at low latitudes, but the COSMIC
171 data show a significant spurious three-peak structure (Yue et al., 2010). To solve this
172 problem, we will use a combination of the International Reference Ionospheric (IRI)
173 model results at the E-layer and IGGM data near the peak height. The low-altitude
174 ionosphere of E layer is mainly controlled by photochemical process, and IRI-2012
175 model (Bilitza et al., 2014) can give more accurate results. The radio occultation data
176 near and above the peak height are also more accurate. Therefore, IRI-2012 model
177 results at heights of 100 km – 140 km will be used, IGGM model results above
178 hmF2-30 will be used, and curve fitting method will be used to calculate the electron
179 density between 140 km and hmF2-30. Therefore, the lower boundary of IGGM
180 model is extended from 140km to 100km after combination with IRI model results.

181 **4. Results and Model Validation**

182 The electron density variations of IGGM model without combination with
183 IRI-2012 results is plotted in Figure 3. For comparison, the electron density variations
184 of IGGM model with combination with IRI-2012 results is also plotted in Figure 3.
185 One can find significant error of three peaks at low heights of low latitudes in the

186 IGGM results without combination with IRI-2012 results. After combination with
187 low-altitude data from the IRI2012 model, the IGGM results significantly corrected
188 the spurious three-peak structure below the F2-layer peak height at low latitudes.

189 Figure 4 shows the IGGM modeled NmF2 results at night time (LT=0.0) in
190 March equinox (Doy=82) under low solar activity (F107=80), middle solar activity
191 (F107=130), and high solar activity (F107=180). The IGGM results show significant
192 longitudinal structure of wavenumber-4 in low latitudes under all solar activity
193 conditions from low solar activity to high solar activity. The longitudinal
194 wavenumber-4 variation is more prominent in low solar activity. In addition, the
195 IGGM model results show significant Weddell Sea Anomaly (40°-60° S latitude and
196 75°-120° W longitude) with electron density enhancements in nighttime. Many
197 previous studies reported such a night enhancement at middle latitudes (e.g. Chang et
198 al., 2015; Chen et al., 2016; He et al., 2009; Jee et al., 2009; Klimenko et al., 2015).
199 Our model results also shows more remarkable enhancement in higher solar activity.
200 The IGGM model results also illustrate the significant ionospheric middle trough
201 structure with a minimum at geomagnetic latitude 50°-70° at nighttime. The peak
202 latitudes have no solar activity dependence, which is consistent with previous studies
203 (e.g. Le et al., 2016; Yang et al., 2015). Figure 5 illustrates the model results in
204 daytime (LT=12) in March equinox (Doy=82) under low solar activity (F107=80),
205 middle solar activity (F107=130), and high solar activity (F107=180). we also can
206 find the significant longitudinal wavenumber-4 structure.

207 IGGM model is not only a model of geomagnetic quiet period, this model takes
208 Kp as geomagnetic activity index and considers the influence of different
209 geomagnetic activities. In order to test the effect of this model on geomagnetic
210 activity simulation, we also established a model without considering geomagnetic
211 activity. Figure 6 shows the relative error of NmF2 in high geomagnetic activity
212 (Kp>3) of the IGGM results with considering Kp and without considering Kp. By
213 comparing the model errors with and without the influence of geomagnetic activity,
214 we find that the IGGM model can significantly reduce the model errors by
215 considering the influence of Kp, especially the larger error rate. The average absolute

216 relative error decreases from 33% of the Kp effect not taken into account to 20% of
217 the Kp effect included. The rate of percentage error of 95% decrease from 1.41% to
218 0.62%. Ionospheric disturbances or ionospheric storms have very complex temporal
219 and spatial variations during geomagnetic activity. IGGM model can only give the
220 average variation characteristics of geomagnetic disturbances. Nevertheless, the
221 model can give the ionospheric disturbances in different regions roughly.

222 To further verify IGGM model results, we selected two types of observation
223 results and an empirical model (IRI-2012) for comparative analysis. The two
224 observations are ZH01 occultation observation and ROCSAT-1 in-situ observation.
225 ZH01 satellite has a similar orbital altitude to COSMIC satellite. Therefore, ZH01
226 occultation observations should be close to COSMIC occultation results. ZH01 is a
227 sun-synchronous satellite with only two local time intervals (1400 LT and 0200LT).
228 This study mainly uses the 1400 LT results. Figure 7 shows the comparison between
229 NmF2 calculated by IGGM model and ZH01 satellite observation results, as well as
230 the comparison with IRI-2012 model results. It is clear from these comparisons that
231 the NmF2 calculated by the IGGM model is very close to the ZH01 observations in
232 terms of latitude variation and longitude structure. However, the results calculated by
233 IRI-2012 are quite different from those observed by ZH01 in both latitude variation
234 and longitude structure. Table 1 shows the detailed comparison of error of NmF2
235 between IRI model results and ZH01 observations and between IGGM model results
236 and ZH01 observations. The percentage error of IGGM model is $\sim 10\%$ at low
237 latitudes and $\sim 20\%$ at middle latitudes. But that of IRI-2012 model is more than 40%
238 at both low latitudes and middle latitudes.

239 Figure 8 shows the comparison between hmF2 calculated by IGGM model and
240 ZH01 satellite observation results, as well as the comparison with IRI-2012 model
241 results. The comparisons show that the hmF2 of IGGM model is very close to that of
242 the ZH01 observation. But there are significant differences between the IRI model
243 results and the ZH01 observation. The detailed differences of hmF2 are listed in Table
244 1. The hmF2 error of IGGM model is larger (~ 20 km) at low latitudes and smaller at
245 (less than 15 km) at middle latitudes. The hmF2 error of IRI model has no latitude

246 dependence. It is larger than 30 km at all latitudes. The results as illustrated in Figures
247 7 and 8 suggest that the IGGM model can well reproduce the major features of
248 ionospheric F2 layer observed by ZH01, but IRI model does not reproduce the
249 observation well.

250 The IGGM model covers an altitude range of 100-700 km. ROCSAT-1's orbit
251 height is about 600 km. Thus, ROCSAT-1 observations of electron density in the top
252 ionosphere were selected to further check the IGGM model's ability to simulate the
253 top ionosphere. First, we compared the global distribution of ROCSAT-1 electron
254 density in different seasons with that of IGGM model and IRI model. The
255 comparisons are shown in Figure 9. The results of IGGM model and ROCSAT-1 have
256 almost the same longitude variation, but the latitude structure of low latitude is
257 slightly different. ROCSAT-1 observations show that the electron density at 600km
258 still has two peak structures at some longitude sectors, but the IGGM model shows a
259 single peak structure. The IRI model also shows a single peak structure. Figure 10
260 shows the comparison of local time and latitudinal variation of ROCSAT-1 electron
261 density with that of IGGM model and IRI model. It is clear that the IGGM model's
262 latitudinal variation and local time is more close to the observations of ROCSAT-1
263 than IRI model's result.

264 A major difference is that the electron density values in the IGGM model are
265 lower than those observed in ROCSAT-1. The electron density value of IRI mode is
266 also lower than the ROCSAT-1 observation, but the same as that of IGGM model.
267 There are two possible reasons for this difference. On the one hand, ROCSAT-1
268 observation period was from 1999 to 2004, while COSMIC data used for IGGM
269 modeling covered 2006-2019. That is to say, the two data sets are in two different
270 solar activity cycles, and the ionospheric variations in the two solar activity cycles are
271 different. On the other hand, ROCSAT-1 is the total ion density observed in situ, while
272 COSMIC result is the electron density profile of radio occultation inversion. The
273 difference in observation principle and instrument error leads to the difference in
274 electron density. Nevertheless, Figures 9 and 10 show consistent seasonal differences
275 in IGGM model, ROCSAT-1 observation, and IRI model, with the highest electron

276 density in March equinox and September equinox, and the lowest electron density in
277 June solstice.

278 One advantage of using Grid Modelling method to develop global or regional
279 ionospheric models like IGGM model is that there is not much fitting or smoothing in
280 spatial structure. This kind of model preserves more spatial structural features. Based
281 on the same COSMIC radio occultation data, we also established a global ionospheric
282 model by using empirical orthogonal function (EOF) method (Li et al., 2021). Figure
283 11 shows a comparison of the simulation results of the two models. We can see that
284 the longitude structure of IGGM model NmF2 and hmF2 is relatively fine, and the
285 ionospheric wavenumber-4 structure can be clearly seen in NmF2 and hmF2.
286 However, the EOF model does not show a similar structure and the result is more
287 smooth.

288 Finally, we compared the calculated results of the IGGM model with COSMIC
289 data used to build the model, and verify the model's ability to reproduce the observed
290 data. Figure 12 shows histogram distribution of percentage error between IGGM
291 model and all the COSMIC observation data in low geomagnetic activity ($K_p < 3$). We
292 can find the IGGM model can reproduce the observations used in the model very well.
293 The correlation coefficient between model NmF2 and observed NmF2 is more than
294 0.93. The mean of percentage error of NmF2 between model and observation is about
295 15%. The mean of error of hmF2 is about 11 km. The detailed error distribution of
296 NmF2, hmF2, and Ne at heights from 300 km to 700 km is listed in Table 2. The
297 results in Table 2 show that the percentage error decreases with height. About 40-50%
298 of the error value of NmF2 and Ne at fixed height is within 15%. And about 90% of
299 the error value of NmF2 and Ne at fixed height is within 55%. As for hmF2, almost
300 all of the errors are less than 55km, and 70% of the errors are within 15km. In
301 addition, we calculate the daytime (08LT - 16LT) and nighttime (20LT - 04LT) error
302 distributions respectively. Figure 13 illustrates the comparison of of error distribution
303 of NmF2 and hmF2 between IGGM model and COSMIC observation in daytime and
304 in nighttime. The results show that both of the NmF2 error and hmF2 error are
305 significantly lower in daytime than in nighttime. The average error of NmF2 was

306 about 13.9% in the daytime and 20.6% in the nighttime. The average error of hmF2
307 was about 10.5km in the daytime and 14.3km in the nighttime. On the one hand, this
308 may be due to the lower electron density at night, so the percentage error is larger; on
309 the other hand, the nighttime ionospheric behaviors are more complicated and the
310 variations are larger.

311 **5. Summary**

312 Ionospheric empirical models are very useful and important platforms and tools
313 for ionospheric climatology and ionospheric space weather applications. Based on
314 various kinds of ionosphere data and methods, the researchers have constructed many
315 regional and global ionospheric empirical models. The COSMIC occultation satellites
316 have accumulated a large amount of ionosphere electron density profile data over a
317 decade of continuous running. Based on these large number of data, we have
318 proposed a new method (Grid Modelling) for modeling the global ionospheric
319 temporal and spatial variations. The core idea of Grid Modeling is to decompose
320 global ionospheric modeling into single grid-point modeling in sufficiently fine grid
321 points. In this way, the spatial structure information can be retained to the maximum
322 extent. In this study, the global ionosphere model was divided into 338,661 grid points
323 with interval of 10 degrees in longitude, 2 degrees in latitude and 5 km in height. Each
324 local grid point model was constructed to model season, local time, solar activity, and
325 geomagnetic variations of ionospheric electron density in each grid point. Then all
326 grid point models are combined to form the IGGM model. The advantage of this
327 modeling is that it only needed to be fitted in temporal variations, not needed to be
328 fitted in spatial variations. Thus it can get more accurate spatial structures of
329 ionosphere.

330 Due to the inherent defects of the algorithm for retrieving ionospheric electron
331 density profile from radio occultation observations, false three-peak structure is prone
332 to appear in the ionospheric data at low latitude. Through data fusion processing with
333 the results of the international reference ionospheric IRI-2012 model, we solved the
334 problem of the forged three-peak structure. At the same time, we further verified the
335 high accuracy of the model in simulating ionospheric spatial structure by comparing it

336 with different data, such as ZH01 and ROCSAT-1 satellite data. Finally, the error
337 analysis between the model results and the observation data used for modeling shows
338 that the error of NmF2 of all data is less than 20%, and the error of daytime is less
339 than 15%, and the error of peak height is less than 13km. IGGM model can output
340 ionospheric climatologic changes quickly and effectively, and it also has many
341 applications in space weather. For example, we are taking IGGM model results as the
342 background field of ionospheric data assimilation, and GPS TEC and occultation TEC
343 data as the observation field to study ionospheric daily variations.

344

345 **Acknowledgement:**

346 We acknowledge COSMIC team for providing the electron density profile data
347 (<https://cdaac-www.cosmic.ucar.edu/cdaac/>). The CSES/ZH01 radio occultation data
348 can be downloaded from the official website (www.leos.ac.cn). The ROCSAT-1 data
349 can be downloaded from the website
350 (<https://cdaweb.gsfc.nasa.gov/pub/data/formosat-rocsat/formosat-1/>). This research
351 was supported by the National Key Research and Development Program
352 (2018YFC1503504), B-type Strategic Priority Program of the Chinese Academy of
353 Sciences (XDB41000000), National Natural Science Foundation of China (41822403,
354 41774165), and Youth Innovation Promotion Association CAS.

355

356

357 **References**

- 358 A, E., D. Zhang, A. J. Ridley, Z. Xiao, and Y. Hao (2012), A global model: Empirical
359 orthogonal function analysis of total electron content 1999–2009 data, *J.*
360 *Geophys. Res.*, 117, A03328, doi:10.1029/2011JA017238.
- 361 Bilitza, D., D. Altadill, Y. Zhang, C. Mertens, V. Truhlik, P. Richards, L.-A.
362 McKinnell, and B. Reinisch (2014), The International Reference Ionosphere
363 2012 - a model of international collaboration, *J. Space Weather Space Clim.*, 4,
364 A07, 1-12, doi:10.1051/swsc/2014004.
- 365 Chang, L. C., H. Liu, Y. Miyoshi, C.-H. Chen, F.-Y. Chang, C.-H. Lin, J.-Y. Liu, and
366 Y.-Y. Sun (2015), Structure and origins of the Weddell Sea Anomaly from tidal
367 and planetary wave signatures in FORMOSAT-3/COSMIC observations and
368 GAIA GCM simulations, *J. Geophys. Res. Space Physics*, 120, 1325–1340,
369 doi:10.1002/2014JA020752.
- 370 Chen, Y., L. Liu, H. Le, W. Wan, and H. Zhang (2016), The global distribution of the
371 dusk-to-nighttime enhancement of summer NmF2 at solar minimum, *J. Geophys.*
372 *Res. Space Physics*, 121, 7914–7922, doi:10.1002/2016JA022670.
- 373 Gowtam, V. S., Tulasi Ram, S., Reinisch, B., & Prajapati, A. (2019). A new artificial
374 neural network-based global three-dimensional ionospheric model (ANNIM-3D)
375 using long-term ionospheric observations: preliminary results. *Journal of*
376 *Geophysical Research: Space Physics*, 124(6), 4639 – 4657.
- 377 He, M., L. Liu, W. Wan, B. Ning, B. Zhao, J. Wen, X. Yue, and H. Le (2009), A study
378 of the Weddell Sea Anomaly observed by FORMOSAT-3/COSMIC, *J. Geophys.*
379 *Res.*, 114, A12309, doi:10.1029/2009JA014175.
- 380 Hedin, A. E., E. L. Fleming, and A. H. Manson (1996), Empirical wind model for the
381 upper, middle and lower atmosphere, *J. Atmos. Terr. Phys.*, 58, 1421 – 1447.
- 382 Hoque, M. M., & Jakowski, N. (2011). A new global empirical NmF2 model for
383 operational use in radio systems. *Radio Science*, 46, 1–13.
384 doi:10.1029/2011rs004807.
- 385 Jee, G., A. G. Burns, Y.-H. Kim, and W. Wang (2009), Seasonal and solar activity
386 variations of the Weddell Sea Anomaly observed in the TOPEX total electron

387 content measurements, *J. Geophys. Res.*, 114, A04307,
388 doi:10.1029/2008JA013801.

389 Klimenko, M. V., V. V. Klimenko, and A. T. Karpachev (2015), Spatial features of
390 Weddell Sea and Yakutsk Anomalies in foF2diurnal variations during high solar
391 activity periods: Interkosmos-19 satellite and ground-based ionosonde
392 observations, IRI reproduction and GSM TIP model simulation, *Adv. Space Res.*,
393 55, 2020–2032, doi:10.1016/j.asr.2014.12.032.

394 Kutiev, I., Marinov, P., Belehaki, A., Reinisch, B., & Jakowski, N. (2009).
395 Reconstruction of topside density profile by using the topside sounder model
396 profiler and digisonde data. *Advances in Space Research*, 43(11), 1683–1687,
397 doi:10.1016/j.asr.2008.08.017

398 Le, H., L. Liu, X. Yue, and W. Wan (2008), The ionospheric responses to the 11
399 August 1999 solar eclipse: Observations and modeling, *Ann. Geophys.*, 26,
400 107–116.

401 Le, H., N. Yang, L. Liu, Y. Chen, and H. Zhang (2017), The latitudinal structure of
402 nighttime ionospheric TEC and its empirical orthogonal functions model over
403 North American sector, *J. Geophys. Res. Space Physics*, 122, 963–977,
404 doi:10.1002/2016JA023361.

405 Lei, J., et al. (2007), Comparison of COSMIC ionospheric measurements with
406 ground-based observations and model predictions: Preliminary results, *J.*
407 *Geophys. Res.*, 112, A07308, doi:10.1029/2006JA012240.

408 Li, Q., Liu, L., He, M., Huang, H., Zhong, J., Yang, N., Zhang, M., Jiang, J., Chen, Y.,
409 Le, H., Cui, J. (2021). A global empirical model of electron density profile in the
410 F region ionosphere basing on COSMIC measurements. *Space Weather*, 19,
411 e2020SW002642, doi:10.1029/2006JA012240.

412 Liu, L., W. Wan, B. Ning, O. M. Pirog, and V. I. Kurkin (2006), Solar activity
413 variations of the ionospheric peak electron density, *J. Geophys. Res.*, 111,
414 A08304, doi:10.1029/2006JA011598.

415 Liu, L., and Y. Chen (2009), Statistical analysis of solar activity variations of total
416 electron content derived at JetPropulsion Laboratory from GPS observations, *J.*

417 Geophys. Res., 114, A10311, doi:10.1029/2009JA014533.

418 Ma, R., J. Xu, W. Wang, and W. Yuan (2009), Seasonal and latitudinal differences of
419 the saturation effect between ionospheric NmF2 and solar activity indices, J.
420 Geophys. Res., 114, A10303, doi:10.1029/2009JA014353.

421 Picone, J. M., A. E. Hedin, D. P. Drob, and A. C. Aikin (2002), NRLMSISE-00
422 empirical model of the atmosphere: Statistical comparisons and scientific issues,
423 J. Geophys. Res., 107(A12), 1468, doi:10.1029/2002JA009430.

424 Schreiner, W. S., S. V. Sokolovskiy, C. Rocken, and D. C. Hunt (1999), Analysis and
425 validation of GPS/MET radio occultation data in the ionosphere, Radio Sci.,
426 34(4), 949–966, doi:10.1029/1999RS900034.

427 Straus, P. R. (2007), Ionospheric climatology derived from GPS occultation
428 observations made by the ionospheric occultation experiment, Adv. Space Res.,
429 39, 793–802, doi:10.1016/j.asr.2006.08.009.

430 Themens, D. R., Jayachandran, P. T., Galkin, I., & Hall, C. (2017). The empirical
431 Canadian high Arctic ionospheric model (E-CHAIM): NmF2 and hmF2. Journal
432 of Geophysical Research: Space Physics, 122, 9015–9031,
433 doi:10.1002/2017JA024398.

434 Titheridge, J. E. (1997), Model results for the ionospheric E-region: Solar and
435 seasonal changes, Ann. Geophys., 15, 63 – 78.

436 Xu, W., and Y. Kamide (2004), Decomposition of daily geomagnetic variations by
437 using method of natural orthogonal component, J. Geophys. Res., 109, A05218,
438 doi:10.1029/2003JA010216.

439 Yue, X., W. Wan, L. Liu, H. Le, Y. Chen, and T. Yu (2008), Development of a middle
440 and low latitude theoretical ionospheric model and an observation system data
441 assimilation experiment, Chin. Sci. Bull., 53(1), 94–101.

442 Yue, X., W. S. Schreiner, J. Lei, S. V. Sokolovskiy, C. Rocken, D. C. Hunt, and Y.-H.
443 Kuo (2010), Error analysis of Abel retrieved electron density profiles from radio
444 occultation measurements, Ann. Geophys., 28, 217–222,
445 doi:10.5194/angeo-28-217-2010.

446 Yue, X., W. S. Schreiner, Y.-C. Lin, C. Rocken, Y.-H. Kuo, and B. Zhao (2011), Data

447 assimilation retrieval of electron density profiles from radio occultation
448 measurements, *J. Geophys. Res.*, 116, A03317, doi:10.1029/2010JA015980.
449 Ikubanni, S.O. and Adeniyi, J. O. (2017), Relationship between ionospheric F2-layer
450 critical frequency, F10.7, and F10.7P around African EIA trough, *Adv. Space.*
451 *Res.* 59(4), 1014-1022
452

453 **Table 1.** Comparison of Error of NmF2 and hmF2 between IRI model results and
 454 ZH01 observations and between IGGM model results and ZH01 observations.
 455

Latitude (°)	Error of NmF2 (%)		Error of hmF2 (km)	
	Error between IRI and ZH01	Error between IGGM and ZH01	Error between IRI and ZH01	Error between IGGM and ZH01
[40 60]	172.1	33.1	52.9	7.1
[20 40]	64.4	12.9	34.4	12.5
[0 20]	47.3	11.8	41.1	21.4
[-20 0]	48.8	10.5	37.3	23.6
[-40 -20]	59.1	22.7	32.1	14.1
[-60 -40]	98.9	25.6	41.1	9.8

456
457

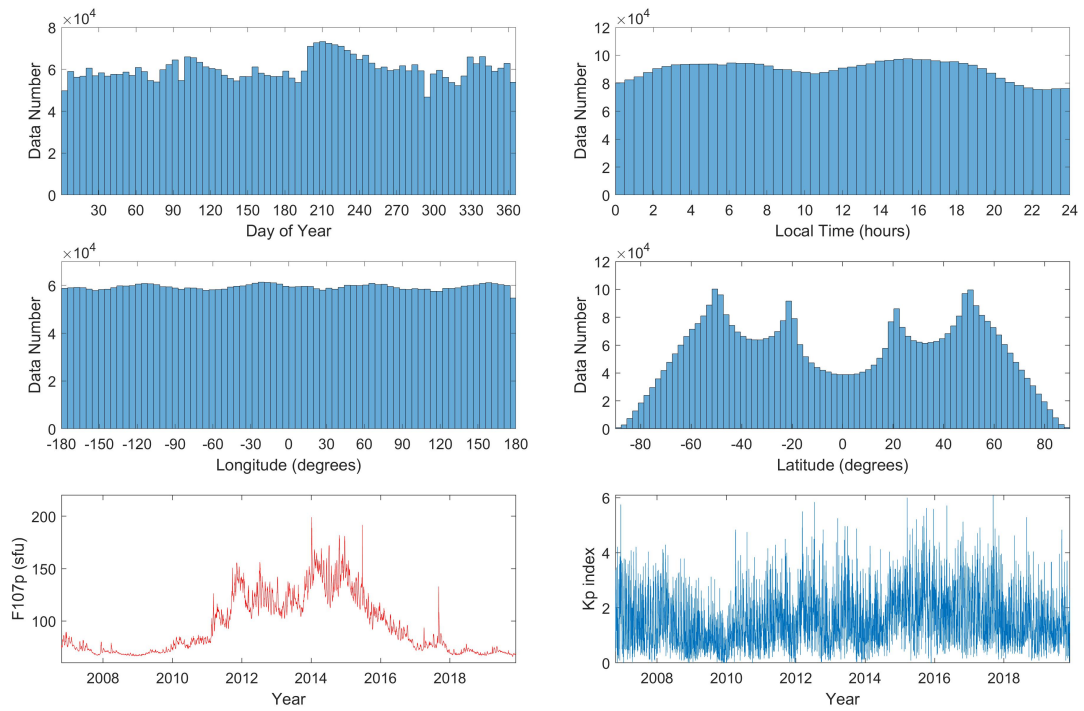
458 **Table 2.** The error distribution of hmF2, NmF2, and Ne at fixed heights of 300km,
 459 400km, 500km, 600km, and 700km.

	mean of absolute error (% or km)	Occurence of error within 15% or 15km	Occurence of error within 25% or 25km	Occurence of error within 35% or 35km	Occurence of error within 45% or 45km	Occurence of error within 55% or 55km
hmF2	11.2	66.1	85.1	93.2	96.7	98.3
NmF2	15.9	47.4	69.5	82.9	89.8	93.3
Ne (300km)	19.2	40.3	61.2	75.3	83.8	88.6
Ne (400km)	18.9	41.1	61.8	75.8	84.4	89.2
Ne (500km)	18.3	42.1	63.2	77.1	85.4	90.1
Ne (600km)	17.7	43.4	64.6	78.4	86.4	91.2
Ne (700km)	17.1	44.1	65.3	79.2	87.2	92.1

460

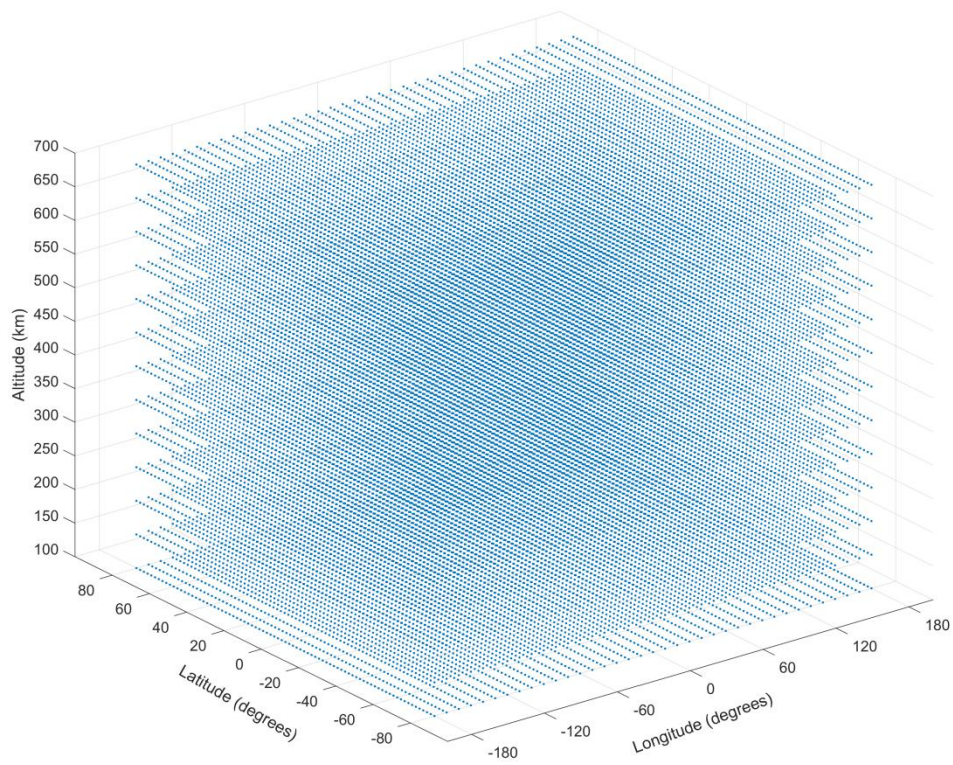
461

462 **Figures**



463

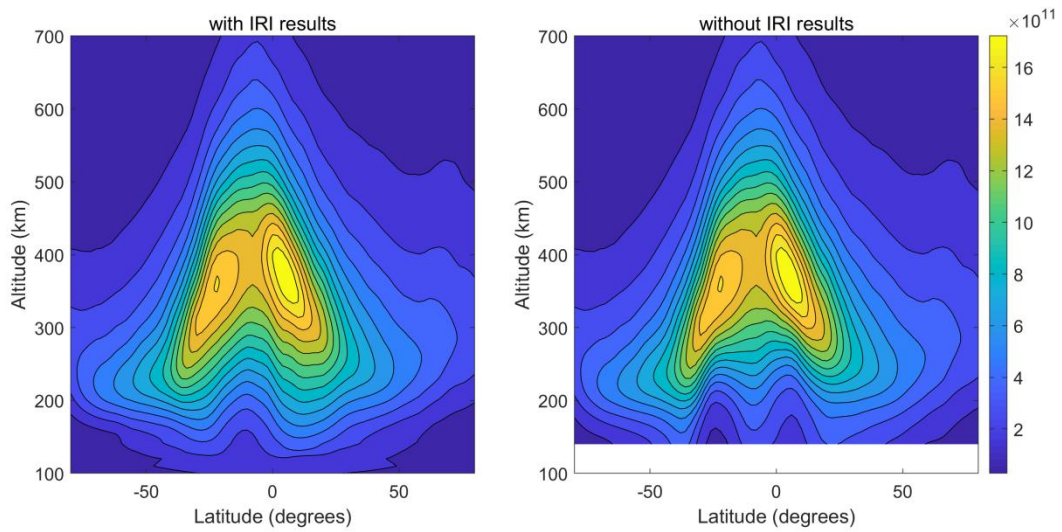
464 **Figure 1.** COSMIC radio occultation data distribution with season, local time,
465 longitude and latitude. Temporal variations of solar activity index F107 and
466 geomagnetic activity index Kp from 2006 to 2019.



467

468 **Figure 2.** Grid point diagram of IGGM model.

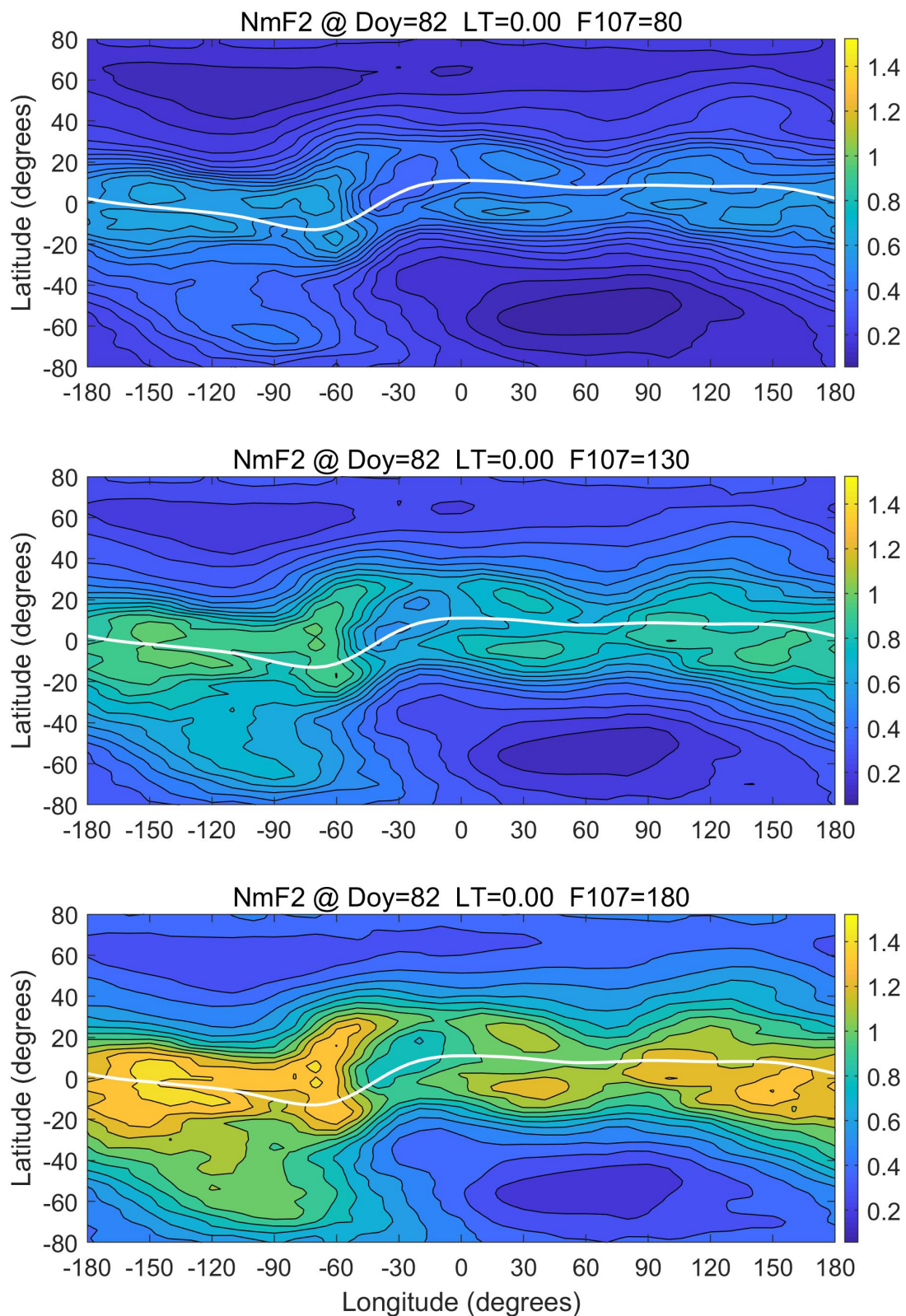
469



470

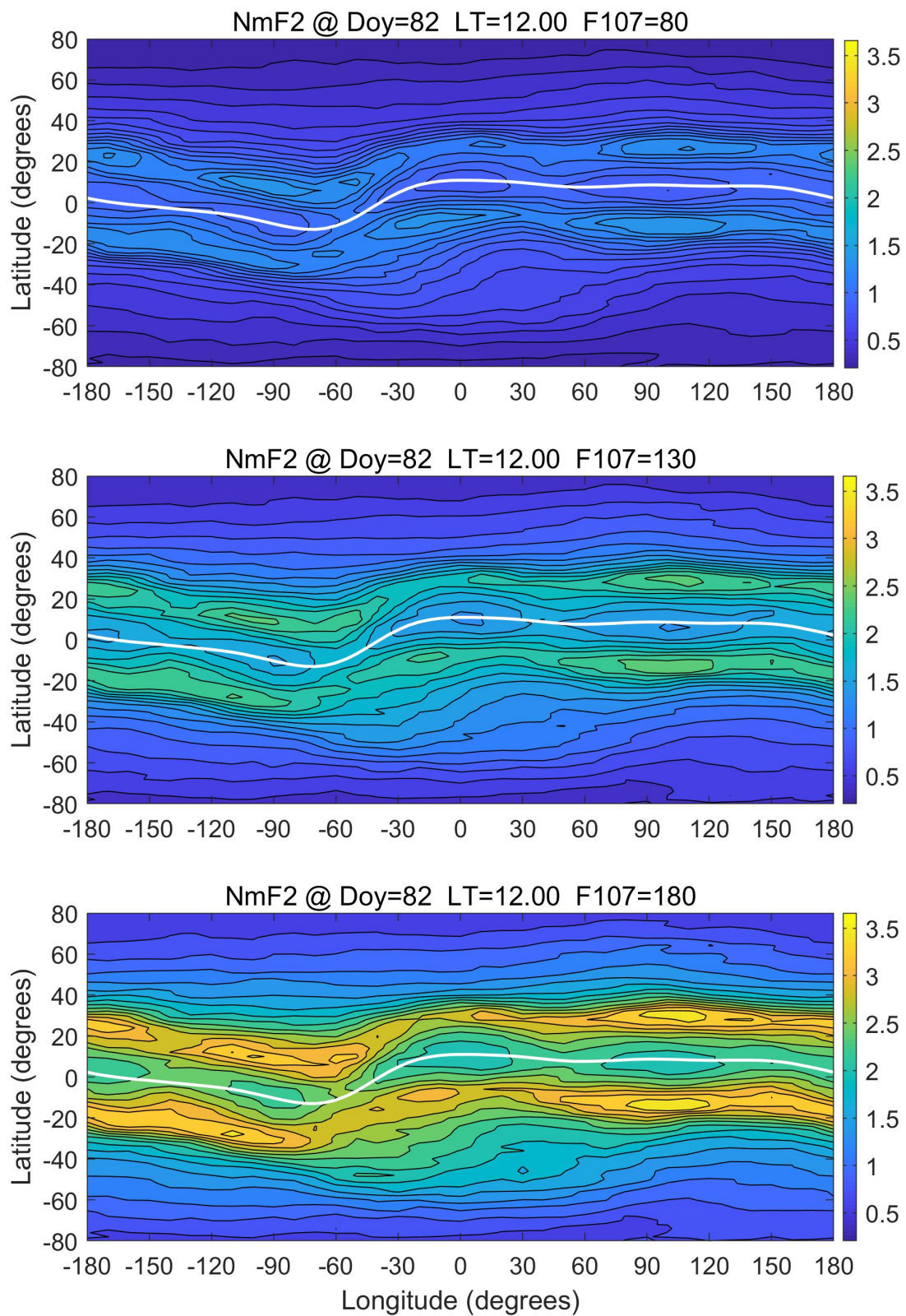
471 **Figure 3.** Comparison of ionospheric electron density height profiles between
 472 combination with IRI model results (left panel) and no combination with IRI model
 473 results (right panel). The figure shows the results of longitude -90° , 1400 LT, march
 474 equinox (DOY=82), solar activity F107=120, and geomagnetic activity $K_p=0$.

475



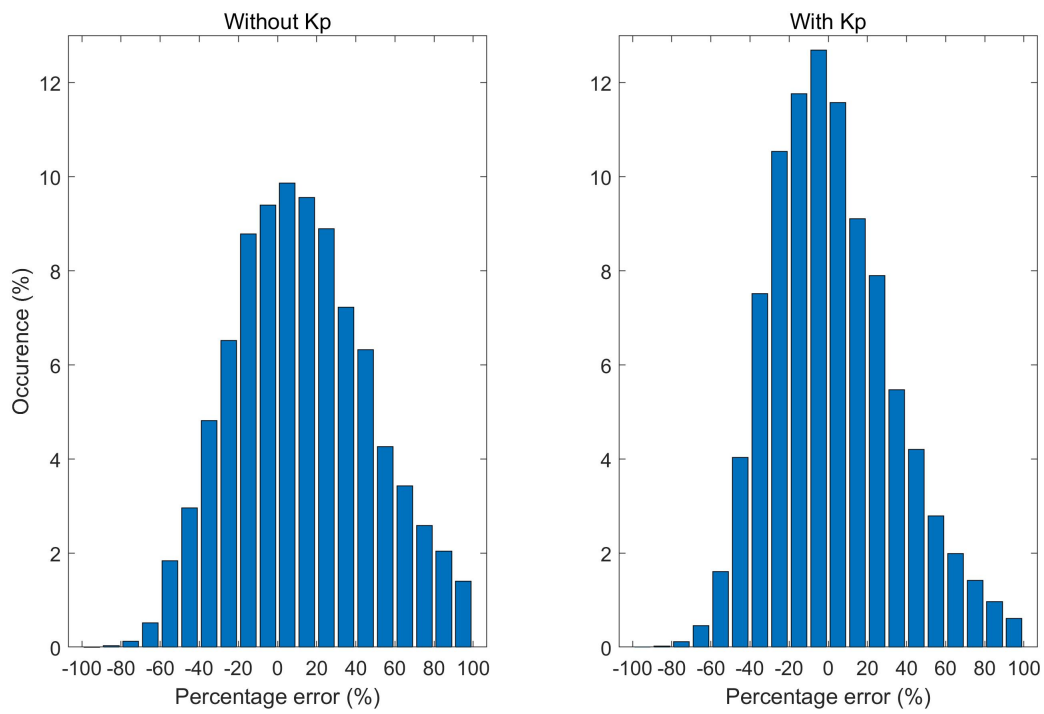
476

477 **Figure 4.** The spatial distribution of IGGM model NmF2 results at LT=0.0 in March
 478 equinox Doy=82 under low solar activity (F107=80), middle solar activity
 479 (F107=130), and high solar activity (F107=180). The unit is 1×10^{12} el/m³.



480
 481
 482

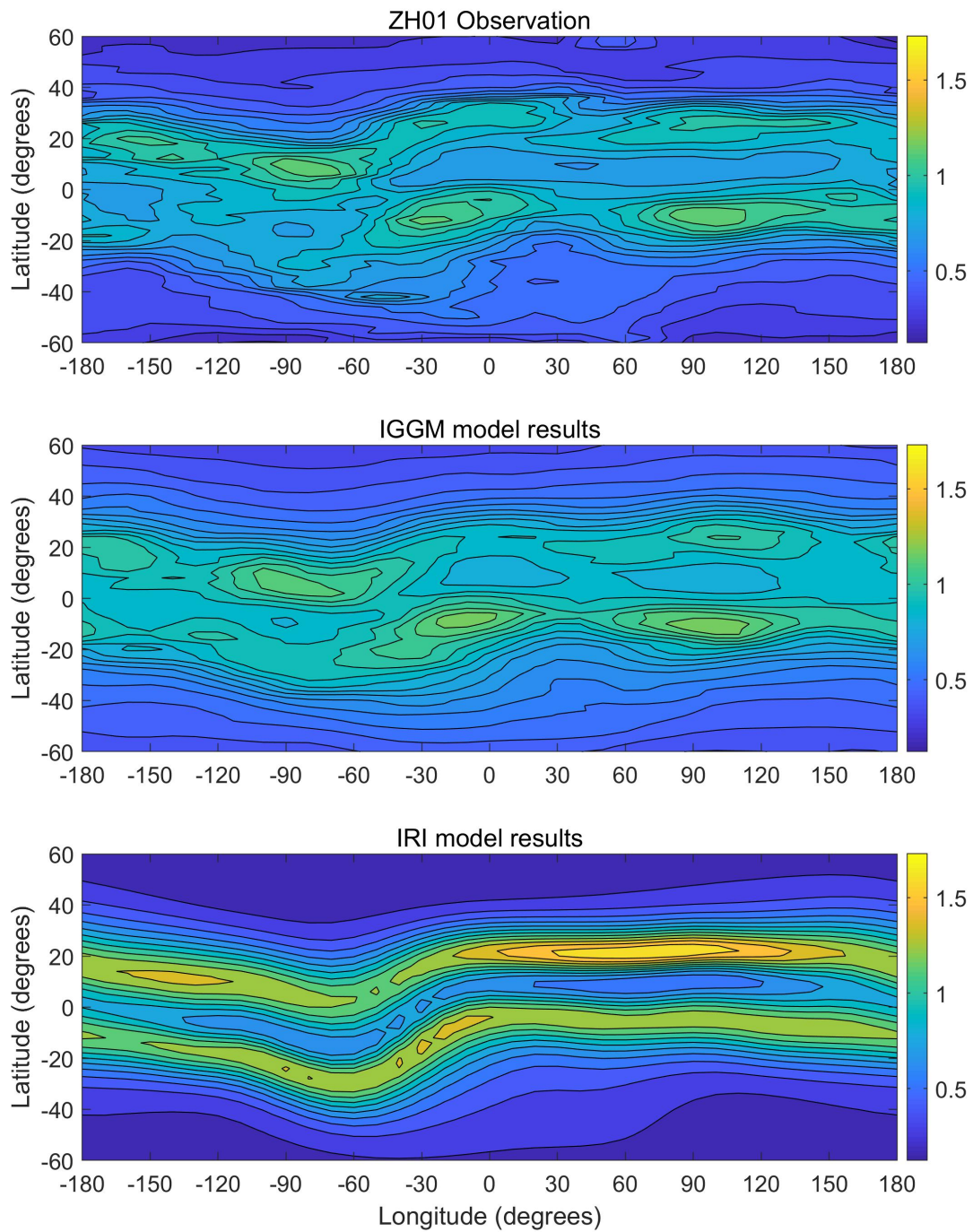
Figure 5. Same as Figure 4, but for daytime LT=12.0



483

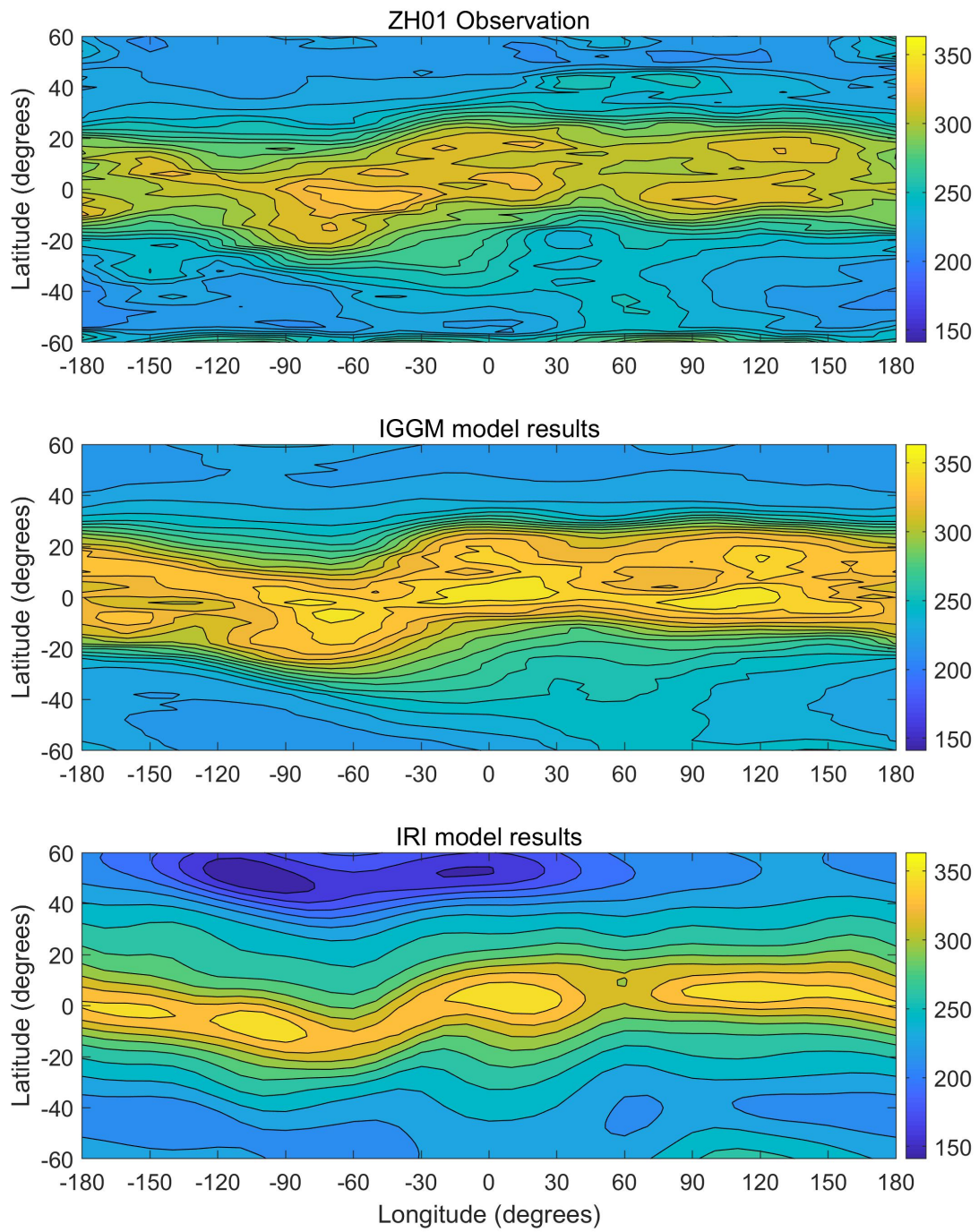
484 **Figure 6.** The relative error of NmF2 in high geomagnetic activity ($K_p > 3$) between
 485 IGGM model results and COSMIC radio occultation observation. Left panel: the
 486 model results without considering Kp's influence. Right panel: the model results with
 487 Kp's influence

488



489

490 **Figure 7.** Comparison of NmF2 of IGGM model results with that of ZH01
 491 observations and IRI model results. The ZH01 results are the 60-day average around
 492 March equinox (DOY 82±30). The modeled local time is 1400 LT, day of year is
 493 DOY=82, solar activity is F107=80. The unit of electron density is 10^{12} el/m³.

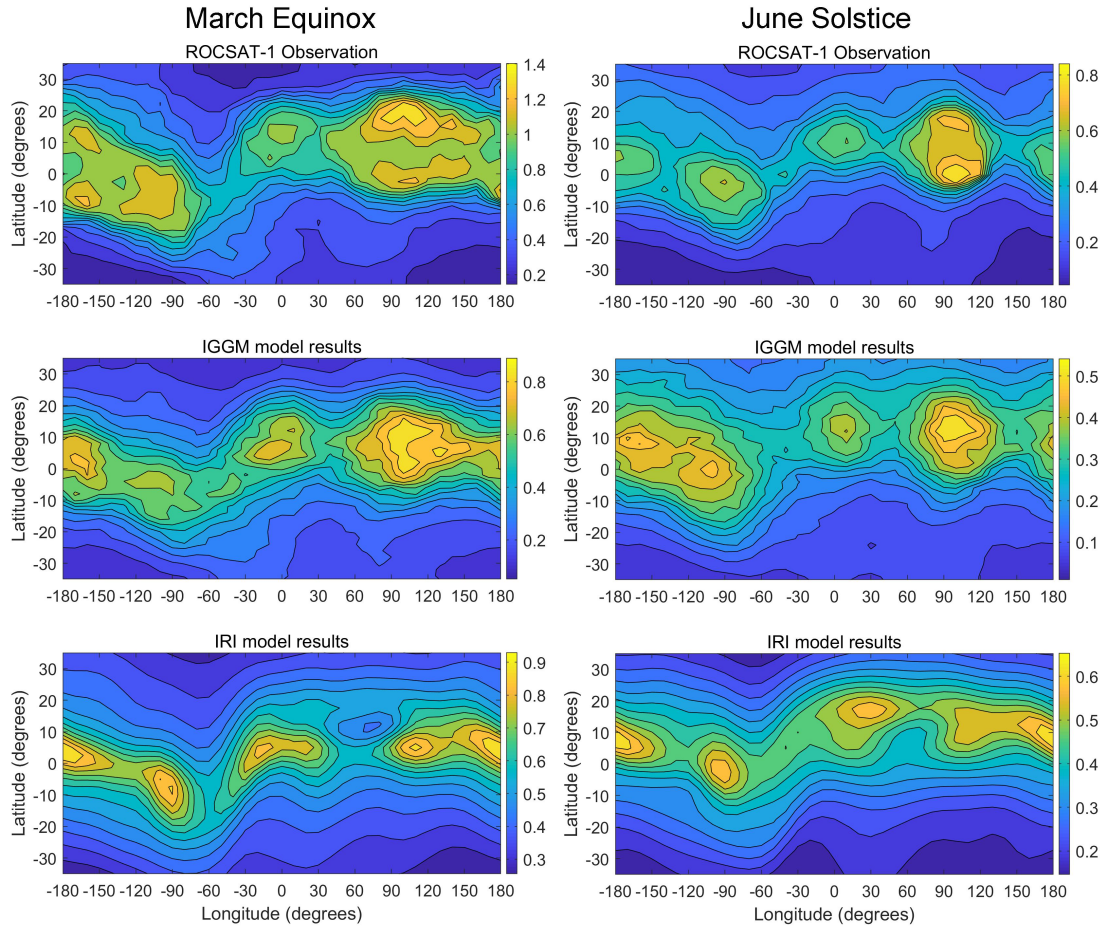


494

495 **Figure 8.** Same as Figure 7, but for hmF2.

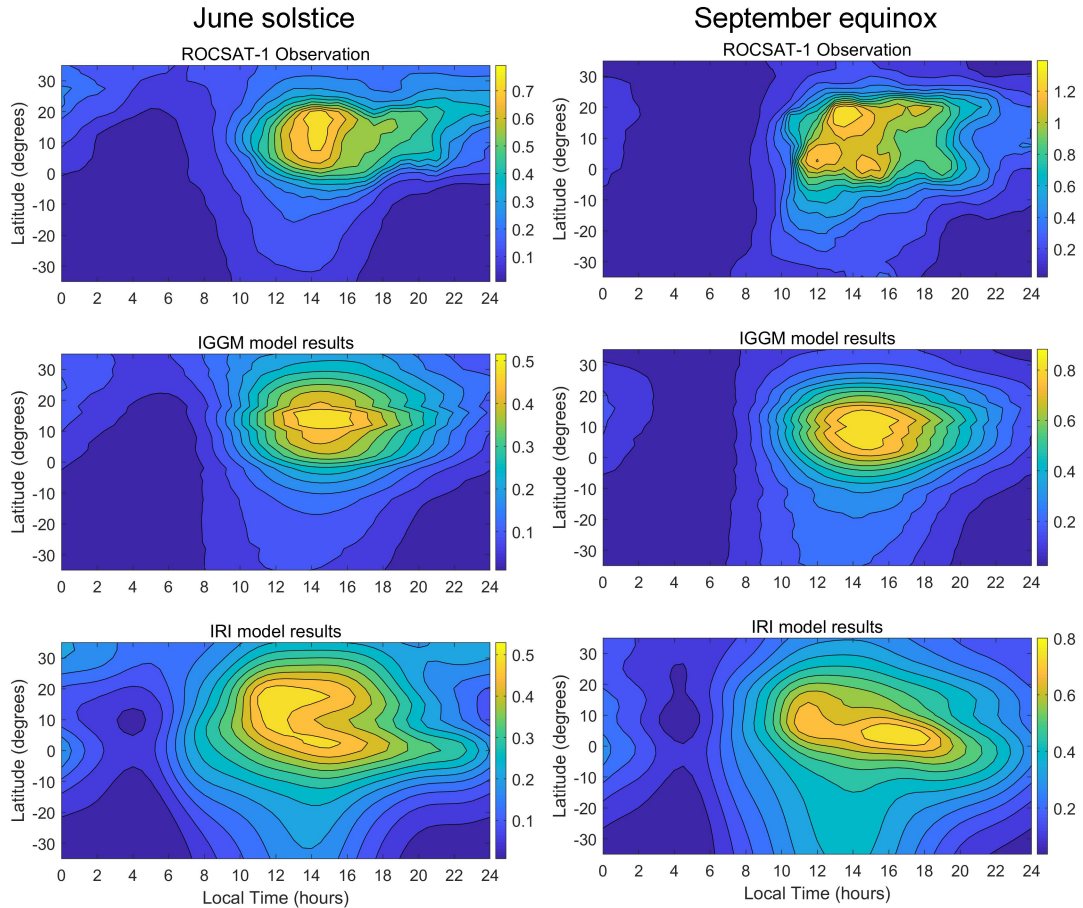
496

497



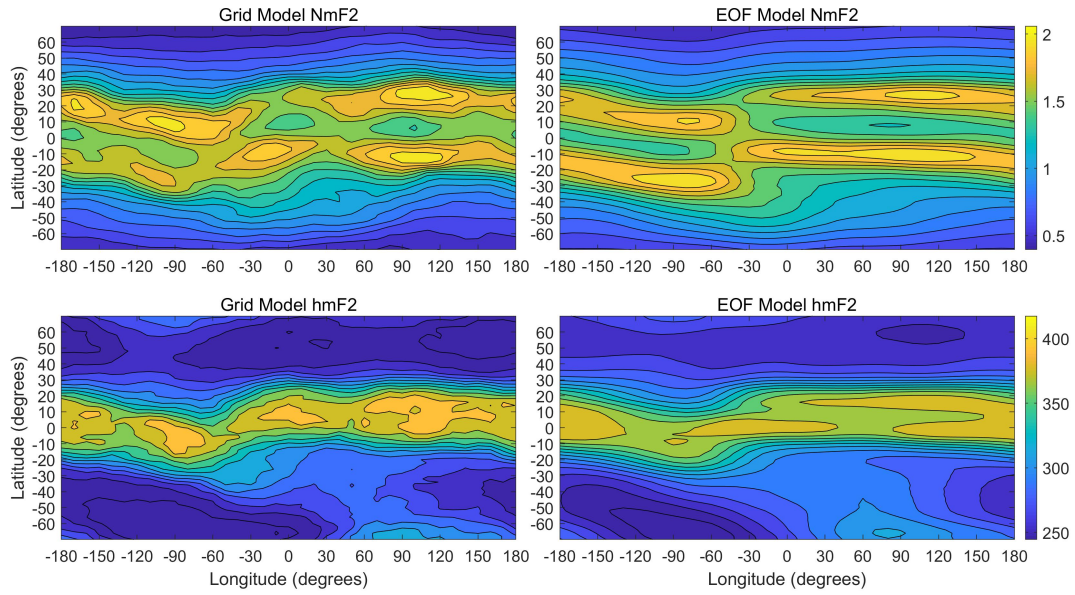
498

499 **Figure 9.** Comparison of topside electron density map of IGGM model with that of
500 ROCSAT-1 observations and with that of IRI model in March equinox and June
501 solstice. The ROCSAT-1 results are the 60-day average around March equinox (DOY
502 82 ± 30) and around June equinox (DOY 173 ± 30). The modeled local time is 1200 LT,
503 height is 600 km, and solar activity is F107=140. The unit of electron density is 10^{12}
504 el/m³.



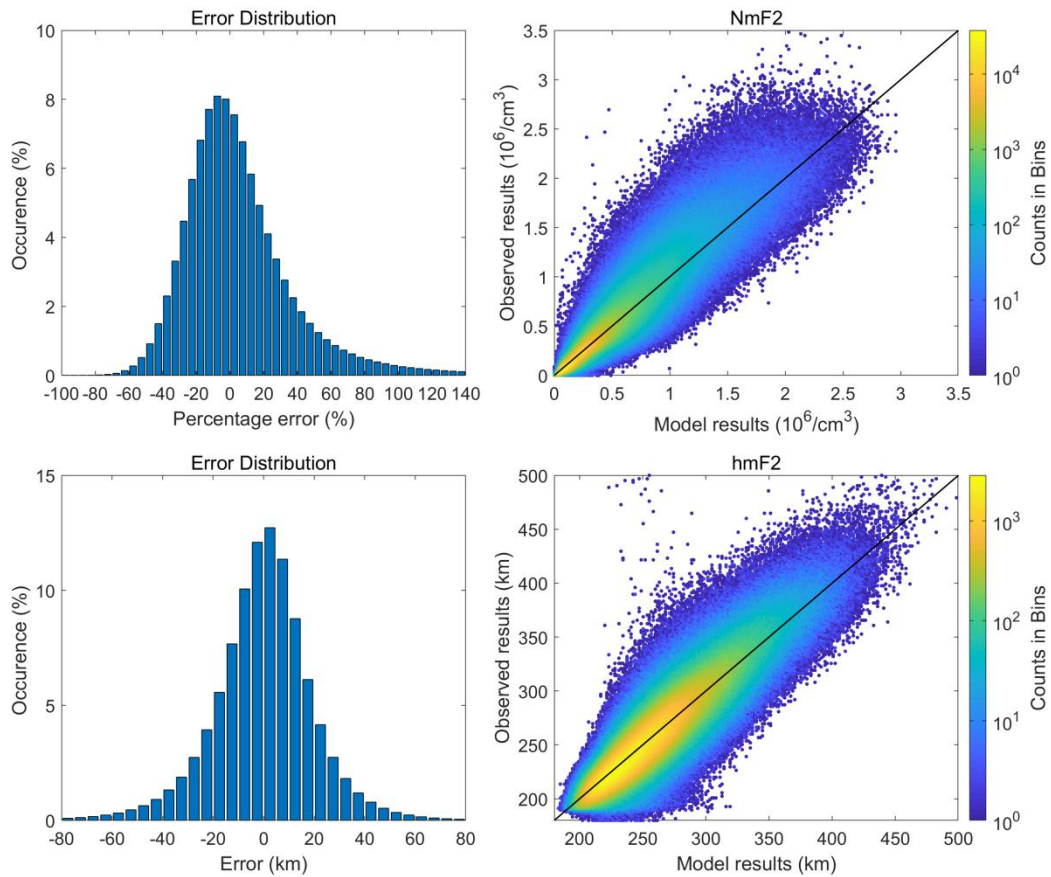
505

506 **Figure 10.** Comparison of topside electron density daily variation of IGGM model
 507 with that of ROCSAT-1 observations and with that of IRI model in June solstice and
 508 September equinox. The ROCSAT-1 results are the 60-day average around March
 509 equinox (DOY 173±30) and around June equinox (DOY 263±30). The modeled local
 510 time is 1200 LT, height is 600 km, and solar activity is F107=140. The unit of electron
 511 density is 10^{12} el/m³.



512

513 **Figure 11.** Comparison of model result of Grid model method with that of EOF
 514 model method. Left panes show Grid model results. Right panels show EOF model
 515 results. The unit of NmF2 is $10^{12}\text{el}/\text{m}^3$. The unit of hmF2 is km. The simulation
 516 condition: DOY=82, F107=120, and LT=12.



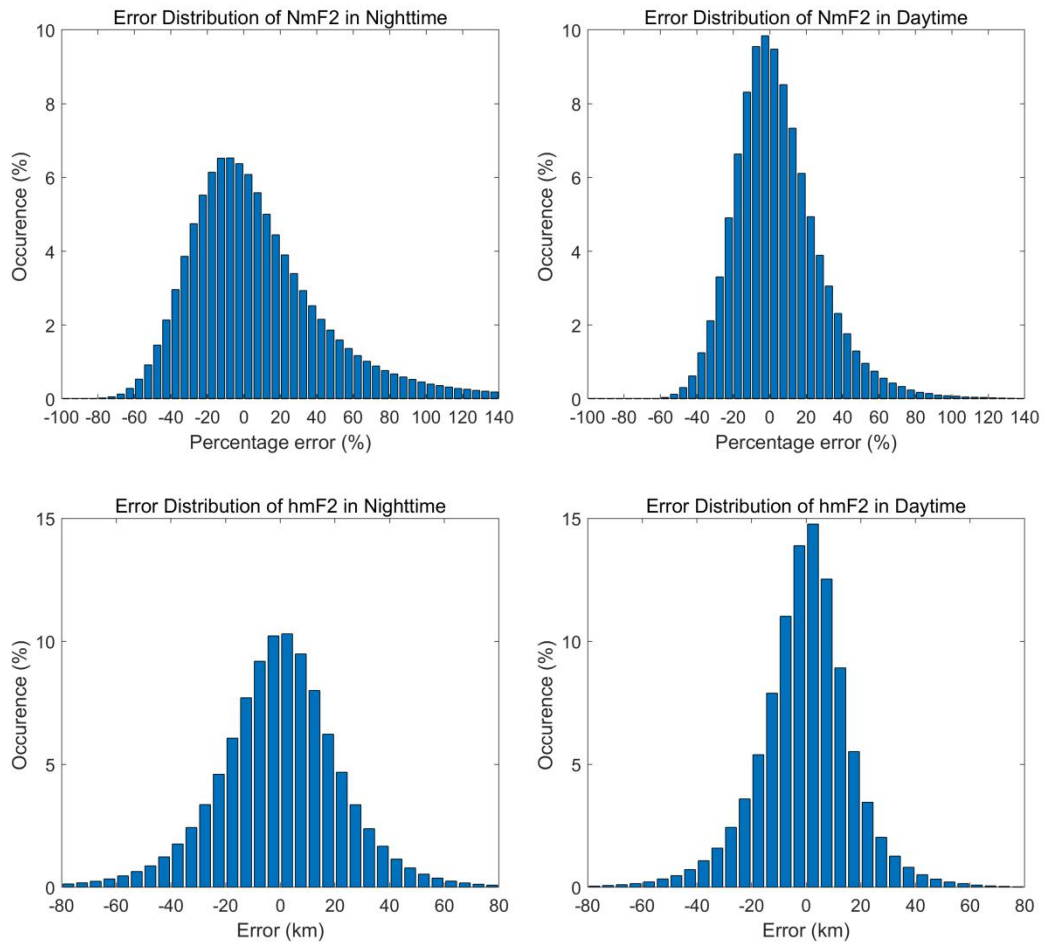
518

519 **Figure 12.** Comparison of NmF2 and hmF2 from IGGM model with that from
 520 COSMIC observations in low geomagnetic activity of $K_p < 3$. (Left panels) The
 521 histogram distribution of percentage error between IGGM model and COSMIC
 522 observation. (Right panels) Bivariate histogram of comparisons between IGGM
 523 model and observations. The solid line shows the linear fitting of model and
 524 observation.

525

526

527



528

529 **Figure 13.** The comparison of error distribution of NmF2 and hmF2 between IGGM
530 model and COSMIC observation in daytime (left panel) and in nighttime (right
531 panel).